Original Article

Compression deformation and fracture behavior of additively manufactured Ti–6Al–4V cellular structures

Yuri N. Loginov [a, b], Andrey Koptyug [c], Vladimir V. Popov Jr. [d, *], Sergey V. Belikov [a], Galymzhan Mukanov [a], Anton I. Golodnov [a], Stepan I. Stepanov [a]

[a] Ural Federal University, 19 Mira St., Ekaterinburg, 620002, Russia
[b] M.N. Miheev Institute of Metal Physics of Ural Branch of Russian Academy of Sciences, Kovalevskaya Str, 18, Ekaterinburg, 620137, Russia
[c] SportsTech Research Center, Mid Sweden University, Akademigatan 1, Östersund, Sweden
[d] Technion - Israel Institute of Technology, 3200003, Haifa, Israel

A B S T R A C T

Corresponding research was carried out to assess if the porous structures with modified diamond-shaped lattice cells can provide better integrity of the constructions in the case of overloading. The aim of the study is designing the structures with high porosity for the biomedical applications (implants) having good load bearing capacity. Studied lattice structures are based on the modified tetrahedral beam-based cells with spherical reinforcements at the beam joints and variable beam diameter. Samples with a porosity of 50–80% were studied in present research. Structures were additively manufactured from a titanium alloy Ti–6Al–4V using SLM. Sample compression tests were carried out according to the ISO 13314 standard. Loading experiments were carried out and critical parameters extracted from the stress-strain curves. Finite element modeling was carried out for the analysis of the stress and assessment of the potential failure mechanisms. Corresponding hypothesis explaining the appearance of shear bands in porous structures under compression is formulated. Obtained results show that when the sample porosity rises from 50% to 80%, corresponding plateau stress decreases by 13 times, first maximum compressive strength decreases by 12 times, and compression offset stress decreases by 12 times, while the plateau end does not change significantly. The experiments revealed the barrel distortion of the samples geometry, which corresponds to the general knowledge how the friction between the solid compressing surfaces (anvils of the compression testing machine) and the lattice affects the sample deformation. Compression experiments also revealed the formation of shear bands during sample deformation. The stochastic nature of their development suggests that the main reason of shear bands appearing is the initial inhomogeneity of the boundary conditions of the experiment.

Suggested modifications of the basic cells show a good potential for achieving regular beam-based lattice structures with high porosity and increased load bearing capacity. More experiments are needed for statistical analysis, and improvements of the loading experiments methodology for better failure mode analysis are planned for the future.

1. Introduction

Choosing the good material to design and manufacture metal orthopedic implants is problematic [1]. Most biodegradable implants are today manufactured from magnesium alloys that decompose *in vivo* [2], while permanent orthopedic implants are predominantly manufactured from titanium [3] or titanium alloys [4–6] as they are sufficiently inert and have high corrosion resistance in various environments. In addition, for the additive manufacturing of implants, CoCr Mo alloy (artificial knee joints) and stainless steel are used [7,8]. Rather limited choice of the metallic materials for the additive manufacturing of biomedical implants is determined by not only the biocompatibility and mechanical properties, but also by the necessary formal approval of the processes (including quality assurance) and facilities [9,10]. Although additive methods are introduced

relatively recently into the manufacturing practice, it is already clear that biomedical applications are among the most significant beneficiaries of their applications along with aerospace and automotive industries. Nevertheless, significant research and development is undertaken optimizing the parameters of the process [11—14], and AM technologies are constantly evolving [15,16].

Beyond the issues of material biocompatibility, solid metallic implants can have other problems, as their mechanical properties may significantly differ from that of the bones they reinforce or substitute. One of the unfortunate possibilities is a risk of secondary fractures at the bone position where the metallic reinforcement ends. It can happen, if the effective Young's modulus of the implant material is much larger than that of the bone it is attached to (in case of fixation plates) or surrounded by (in case of stem type implants). In such case, the bone where the implant ends experiences quite large stress and additional fractures can occur even with supposedly mild loading. Same Young's modulus mismatch can lead to so-called stress-shielding, bone material loss and implant loosening [17]. In both cases, the problem lays with the high stiffness of the implant. One of the ways forward to avoid the stiffness mismatch is using metamaterial approach [18,19], when certain sections of the implant are made porous. Introducing open cell porous structures not only decreases the equivalent stiffness of the implant sections, but also promotes bone ingrowth and thus additionally stabilizes the implant. Porous structures with both regular and stochastically distributed cells are used. Corresponding sections should have sufficient porosity [20], which has an effect on the implant survival rates including the direction and the rate of bone ingrowth [21]. This is confirmed by animal experiments and medical practice [22,23].

Additively manufactured porous structures can be generally categorized into the strut-based lattice structures [18,22,24], and surface-based ones [19,21,25]. Both of these can be basing on regular cell elements (including regular changes to form gradient type structures [18]) or stochastically distributed ones [20]. Application of the metamaterial approach also allows varying the mechanical properties and effective diffusion for example through varying the unit cell shape, dimensions and apparent density [18,19]. Corresponding design of the complicated structures, especially with solid and porous sections with demanded properties strongly depends on advanced computer modeling [26—28] and follow-up testing. Effective elastic modulus, the fracture limit and failure modes are among the parameters critical for the success of the porous structure application [29—31].

A significant number of research papers discuss the internal architecture design of porous metal implants, and their performance under large plastic deformations [32—34]. It was established that the plastic properties of the structures made of Ti—6Al—4V alloy increase if they are obtained using electron beam melting (EBM) compared with the structures obtained using the SLM method [35]. Although these two powder-bed AM modalities are so far dominating in the manufacturing complex structures with porous sections including implants, other methods using powders [36], granules and fibers as the precursor materials [36—38] are becoming available. But all AM methods are dependent on the computer-aided design models [39]. Design of advanced implants is today to a large extent driven by optimizing not only its shape, material, but also essential functionality, which in turn is also majorly performed via computer modeling [10,40].

One of the acute problems related to the performance of the lattice and porous structures is possible localized failure of their elements, often leading to the loss of structure integrity. Possibility of the catastrophic failure of the lightweight (porous) structures from unexpected loading or due to fatigue are as acute for implant applications as for the automotive or aerospace ones. Due to some specific features of additively manufactured porous

structures, such as insufficient ductility of additively manufactured titanium alloys mentioned by some researchers, and certain defects characteristic to additive manufacturing such as significant surface roughness, local lack of fusion, micropores, residual stresses etc. [41]. Additional problems can occur from the loosening of the powder grains partially melted to the structure surfaces, or small debris resulting from partial fracturing of the pore walls or struts. Additional problems can occur with the porous sections of the implants when the solid bone starts to penetrate the outer layers (periphery) of the implants, reinforcing them and generating additional stress at the layers nor reinforced by new grown bone [42].

Therefore, the sufficient ductility as well as the high strength of the implant material are required. Note that one should clearly separate the properties of the structure-at metamaterial level (elastic deformation limit, exceeding the tensile strength, fracture modes, stress fields) from the similar termed properties of the cell elements and solid material. Pure titanium and Ti—6Al—4V (grade 5) are the most commonly used certified materials for additive manufacturing of implants [43].

The purpose of this research is to study the ductility and fracture behavior additively manufactured Ti—6Al—4V samples with the lattice structure based on the modified diamond-shaped (tetrahedral) basic cell elements used for osteosynthesis.

2. Material and methods

Prismatic samples with the size of 30 mm × 20 mm × 20 mm (Fig. 1) were manufactured using selective laser melting (SLM) EOS 280 machine from Ti—6Al—4V (grade 5) alloy powder, supplied by EOS Gmbh, in an argon atmosphere. Corresponding powder is plasma-atomized with near-spherical grain shape. Powder grain size distribution was measured by laser diffraction (ANALYSETTE 22 NanoTec). Corresponding distribution D-values are $D_{10} = 18$ μm, $D_{50} = 34$ μm and $D_{90} = 50$ μm. A number of samples with different porosity were manufactured in a single batch using raster scanning and rotation of scanning direction for 68° between consecutive layers. The rectangular samples for compression tests with the dimensions of 20 mm × 20 mm × 20 mm (length × width × height) were separated from the building platform using electric-discharge cutting. Fig. 1 shows the elemental cells of the lattice structures with different density used in present studies (top row); overall models of the lattice samples with different porosity indicating the dimensions of the cut samples for mechanical tests (middle row); and the overview of the manufactured samples with the supports before removal from the building platform (bottom row).

CAD models of the samples were generated basing on the modified tetrahedral elemental cells using software package SolidWorks by Dassault Systèmes. Files were converted into the standard (.stl) format for SLM manufacturing. The target porosity P of the structures was set to 50%, 60%, 70% and 80% density as calculated according to the expression:

$$P = \left(1 - \frac{\rho_\upsilon}{\rho_t}\right) \cdot 100\% \tag{1}$$

where ρ_υ and ρ_t - the apparent density of porous lattice structure and density of the material from which the implant was made correspondingly. Corresponding apparent density is calculated from the outline dimensions of the sample and its measured mass:

$$\rho_\upsilon = \frac{m}{V} \tag{2}$$
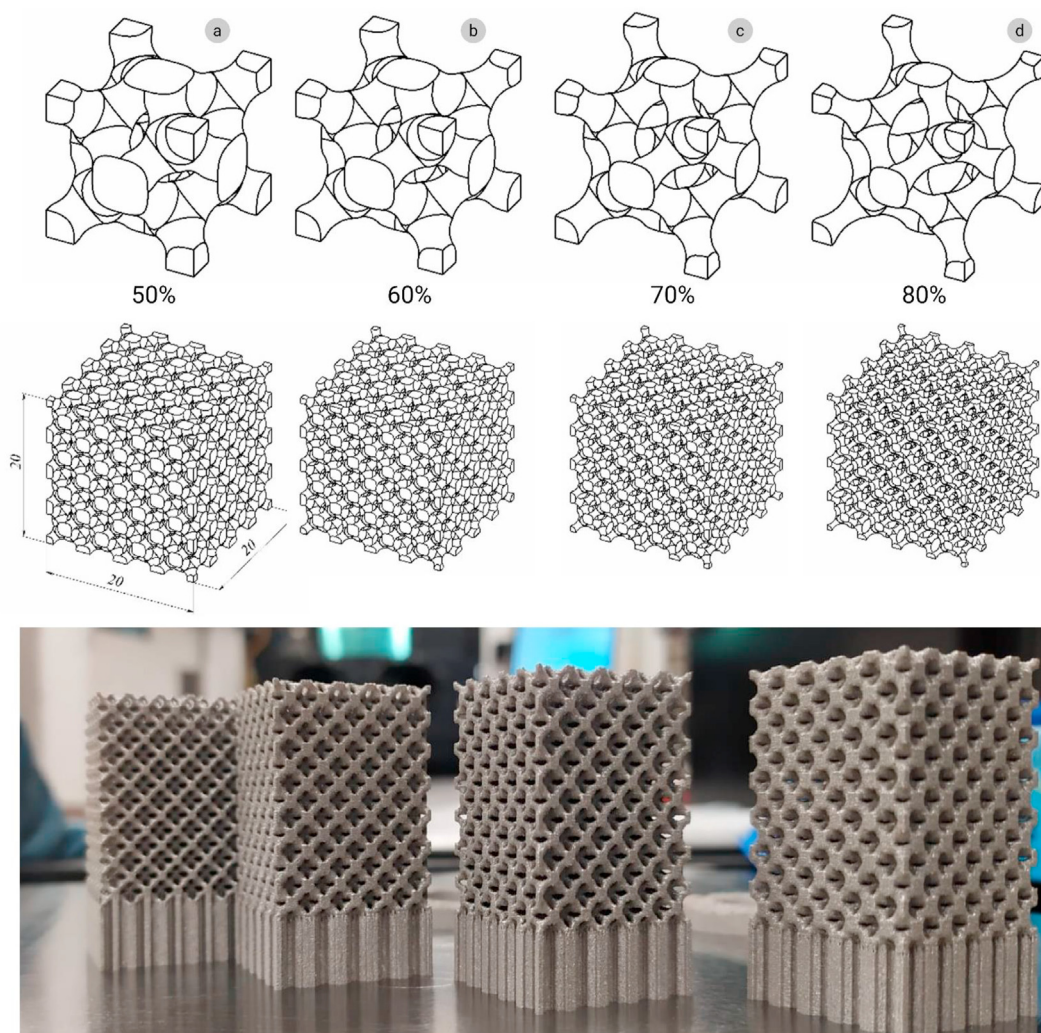
Fig. 1. Elemental cells, models of lattice structures, and additively manufactured samples of these structures with four various density: a − 50%, b − 60%, c − 70%, and d − 80%.

where m and V − the mass and the volume of the porous sample.

Unit cells are designed basing on the round beam-type diamond (tetrahedral) architecture with the beams placed at the angles of 109°28'. Reinforcing elements were introduced with the intention of preventing high stress concentrations at the beam joints. In contrast with many traditional designs based on the unmodified diamond lattice cell elements, the beams are also having particular structure with variable cross section, with the diameter increasing towards the beam joints, attempting to keep reasonably low apparent density of the cells (high porosity of the structure). Additional spherical elements are introduced into the joints. Fig. 2 illustrates overall view and critical cross-sections of the basic diamond (tetrahedral) cell (Fig. 2a) and its modified version (Fig. 2b) used in experiments. Detailed parameters of the elemental cell models for the structures with different design porosity are presented in Table 1.

The density of the specimens was studied by the hydrostatic method using Archimedes' principle according to ASTM B311-17 at Israeli Institute of Metals (IIM). Measurements were carried out using distilled water as the fluid with a resistivity of 50 MΩ*cm at 22 °C for 2 h for each measurement (without adding a surfactant). The Density Kit, METTLER TOLEDO (Switzerland) precision balances with 0.1 mg readability was used for this purpose. The system was placed in air-conditioned laboratory (21±1°C) with controlled

humidity of 55%. There were 3 samples of each type (with a porosity of 50%, 60%, 70%, and 80%).

3. Results and discussion

3.1. Density of the samples

The density of the 36 mm × 25 mm × 250 mm lattice structured samples was measured using Archimedes' method.

The Archimedes method is a well-known and commonly used for density measurements in case of both solid and porous samples. However, it should be taken into account, that this method does not give any information on the character of material porosity, and might be not accurate because of the partially fused powder particles on the metal surface or other morphological defects [44]. Lattice samples with high surface to volume ratio may be quite problematic in this respect, as the amount of small crevices and gaps between the fused grains and their surface, where the air pockets can remain, may decrease the precision of Archimedes' method measurements.

Table 2 presents the results related to the mass, volume, and density of the lattice samples. The Table 2 also presents the deviation of the values measured for additively manufactured samples from the ones calculated from the used CAD models. Due to
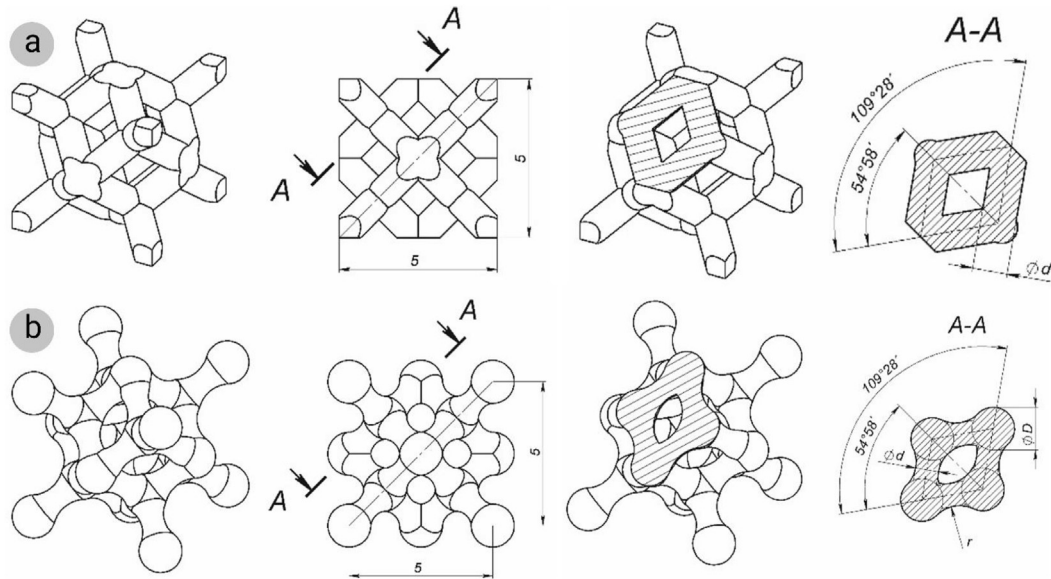
Fig. 2. Design evolution of the diamond type unit cell: a − original basic cell layout; b − modified cell with the beams of variable cross-section and reinforcing spherical elements placed in the beam joints, used in the experiments. In the figures left to right: overall view of the cell; side view of the cell with dimensions and marked cross-sectional plane: view of the cell cut in the cross-sectional plane; dimensions of the elements in the cross-sectional plane and parameters *D*, *d* and *r* defining cell modifications.

Table 1
Parameters of diamond lattice structure with different porosities.

Sample	Pore fraction, %	D, μm	r, μm	d, μm
1	50	1880	920	1200
2	60	1720	1020	1020
3	70	1520	1120	820
4	80	1280	1240	600

D-diameter of the spherical reinforcing elements; *r*-curvature radius of the beam tapering; *d*-minimal diameter of the beam (see Fig. 2b).

relatively small numbers of measured samples, and potential issues with Archimedes method measurements of the lattice samples with high surface roughness and very high surface to volume ratio, only the average values for three samples of the same porosity are presented.

The results obtained by Archimedes' method indicate that all the samples have high material densities between 98.2% and 99.5%, which corresponds to the values reported in the literature [44,45]. Results also indicate relatively small deviations in geometry between the manufactured samples and CAD models, with some tendency of growing deviation with increasing pore fraction.

3.2. Compression testing

Compression tests of the samples were performed according to the ISO 13314 standard [46]. Fig. 3a illustrates corresponding setup for the tests with the sample placed between two anvils. The method involves analyzing the dependence of the loading force vs.

anvil displacement. Fig. 3b presents a typical stress-strain curve recorded in such experiments.

Fig. 4 presents the result of modeling of equivalent strains for the cross-section coming through the central plane of the sample. Blue zones represent the anvils of the compression-testing device. The zone of small deformations of the sample adjoins the anvils and has a wedge-shaped form. Typically, such a zone in forged solid samples is associated with a hindered deformation zone. A higher level of deformations was noted on the lateral surface of the sample and in the center. The inhomogeneity of the strain distribution for cellular materials was also noted in other works [47].

According to Ref. [48], corresponding results can significantly vary depending on the material, type of the porous structure, and apparent density. The methodology assumes that corresponding engineering stress dependencies are calculated using the expression $\sigma = F/A_0$, where A_0 is the initial area of the sample contact surface.

Corresponding shear strain is calculated using the expression $\varepsilon = 100 \cdot \Delta h/h_0$, where h_0 is the initial height of the sample and Δh-change in the height at certain load. Majority of modern test devices perform such calculations automatically.

Further text contains some of the following abbreviations used by the above-mentioned ISO standard:

- σ_{max1} - first maximum compressive strength;
- σ_{pl} - plateau stress - the average stress in the compression interval of 20−30% or 20−40% (the interval depends on the length of the plateau);

Table 2
Volume deviation between the theoretical (CAD) and experimentally measured Archimedes' method for the additively manufactured lattice samples with different pore fractions.

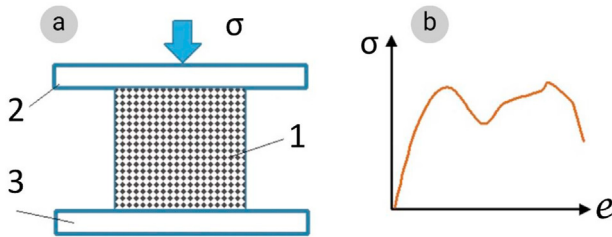| Sample	Pore fraction, %	Mass in air (mg)	CAD dense volume (mm³)	CAD lattice volume (mm³)	Mass in water (mg)	Archimedes lattice volume (mm³)	Deviation CAD/Archimedes volume (%)
1	50	45.981	21,875	10852.224	35.436	10,568	2.67
2	60	37.932	21,875	8783.263	29.319	8632	1.75
3	70	28.382	21,875	6623.996	21.959	6437	2.91
4	80	19.029	21,875	4505.361	14.716	4323	4.22

Fig. 3. (a) Cellular sample compression according to Ref. [46], (b) typical compression curve, where σ is the stress and e is the strain.
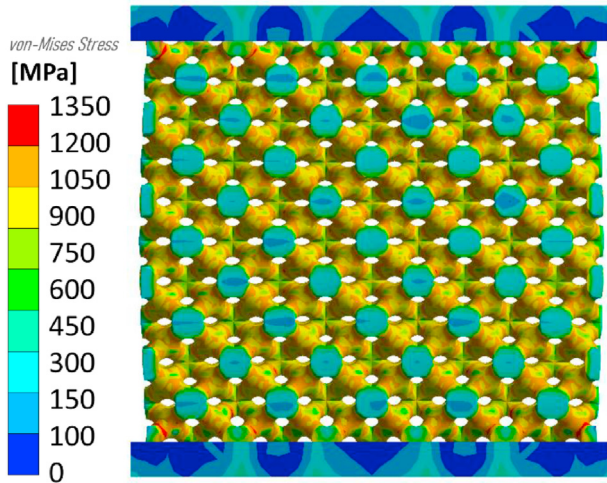

Fig. 4. Distribution of von-Mises equivalent stresses in vertical cut-plane.

- e_{pl} - plateau end strain. The end point of the plateau — the point on the diagram where the stress is 1.3 times higher than the σ_{pl};
- $\sigma_{0.2}$ - compressive offset stress - compressive stress at the plastic compressive strain of 0.2%.
- W - energy absorption;
- W_e - energy absorption efficiency.

The sample was compressed using an Instron 3382 testing machine with the displacement rate 1.8 mm/min. The process was video recorded (see Data availability statement); all the displacements, strains and stresses were monitored by the test machine.

3.3. Modeling compression of the structures

The FEM simulation of compression loading of prismatic lattice structure having 60% porosity was performed in the Mechanical Structure module of ANSYS software. The boundary conditions are chosen to mimic the conditions imposed by the test machine used for compression testing, with top and bottom anvils parallel and moving towards each other. The formal boundary conditions are specified as follows: the lower layer is fixed and has no displacements in the horizontal plane (fixed support); the compression was controlled by the anvil displacement of 2 mm. Anvil material properties were set basing on the parameters of a structural steel with the Young's modulus increased by three orders of magnitude considering the anvil as a rigid body. It allows excluding the elastic deformation of the anvil and they can be neglected during the modeling. The properties of the lattice material was selected from the 'Engineering Data Sources Additive Manufacturing Materials - Ti−6Al−4V' library integrated in ANSYS software. The properties of the material are defined as follows: density - 4430 kg/m³; modulus

of elasticity −114 GPa; Poisson's ratio - 0.323. The contact between the sample and the plates from both edges was set taking into account friction in accordance with the Amontons-Coulomb law:

$$\tau = \mu_p * p \tag{3}$$

where $\mu_p = 0.3$ − friction coefficient.

Modeling solution is represented in a form of equivalent stress distribution, which reach values of 1200 MPa in the local regions (Fig. 5). The side surfaces of the sample were barreled similar to the experiments, which is explained by the friction between the plates and the sample. An enlarged image of the contact zone with the field of equivalent stresses (see Fig. 6d) allowed us to establish that the maximum stresses are located on the periphery of contact region.

3.4. Results of the compression tests

Behavior of the samples with 60% and 70% porosity under compression was quite different. Fig. 6 presents typical results for the compression of the sample with 60% porosity. In the course of the deformation, the near-round pores of the samples (Fig. 6a) transformed into the oval ones (Fig. 6b). At a certain point of the compression, a thickening zone having about 15° inclination to the plates was observed (arrow in Fig. 6b). Substantial deformation was localizing in this zone at later compression stages. The cells in the peripheral upper and lower zones remained almost round (Fig. 6c). This continued until the sample periphery started to crumble (Fig. 6d).

The pores of the sample with 70% porosity are larger than those of the sample with 60% porosity (Fig. 7a). Similar to the previous case, at the initial compression stages pores were deforming from rounded to oval (Fig. 7b). The thickening zone had a greater angle of inclination (almost 45°) to the compression plates (Fig. 7c). At later stages, the deformations remained localized in this zone. As in previous test, the crumbling of the structure happened at one of the sides in the damage localization zone (Fig. 7d).

In the described samples, only small barrel distortion of the edges was observed, which was some more pronounced for the sample with 70% porosity. It should be also noted, that in both cases there were no failure of the sample along the localized damage plane and the samples kept their relative integrity without separating in halves.

3.5. Compression stress-strain diagrams

Fig. 8 presents typical dependences of engineering stress on compressive strain for all tested samples with different porosity.
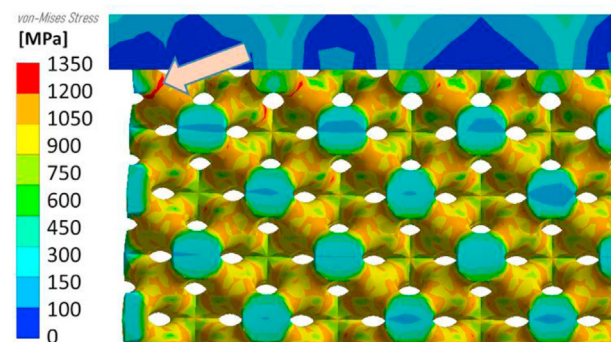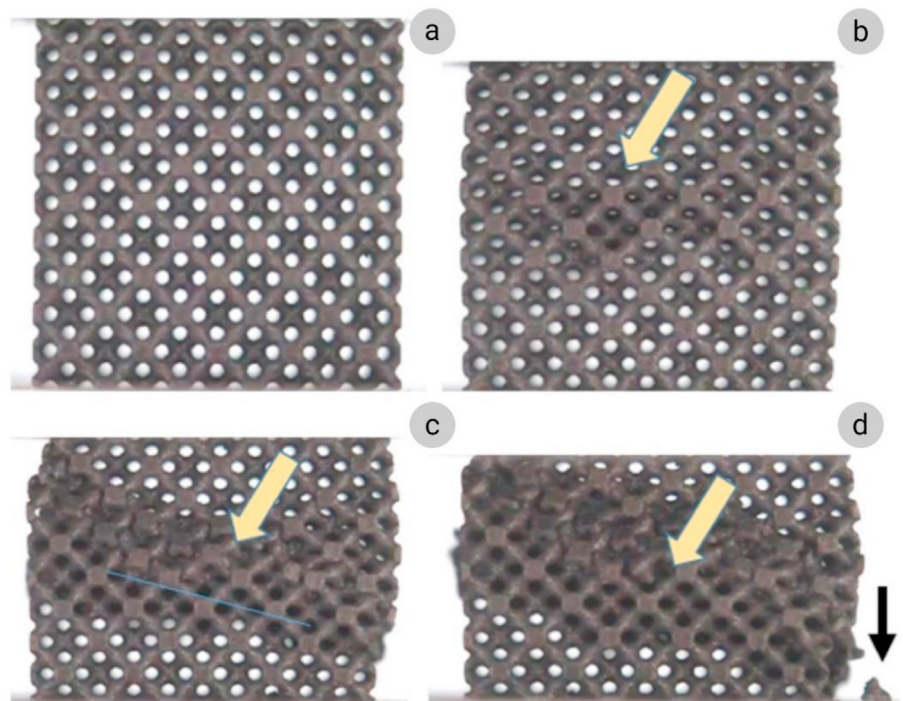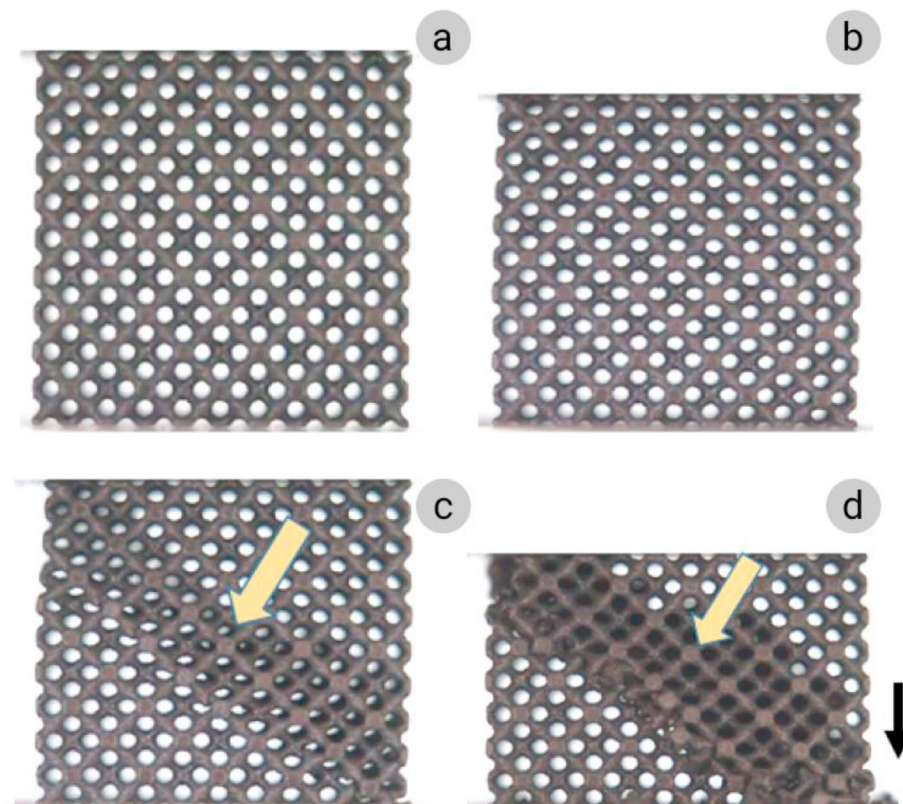

Fig. 5. The distribution of equivalent stresses in the contact region. An arrow marks the area of maximum stresses.

Fig. 6. Compression test of the sample with 60% porosity: a-initial state; b - emergence of a zone with localized deformation (arrow); c - development of the zone of localized deformation and formation of the crashed cell zone; d-crumbling of the sample.

Fig. 7. Compression test of the sample with 70% porosity: a-initial state; b − emergence of the deformation in the pore shape; c-development of a zone with localized deformation (arrow); d-crumbling of the sample.

Characteristic shapes of the dependencies are very similar in all cases. The first maximum compressive strength follows the elastic loading region. Its value as expected is smallest for the samples with highest (80%) porosity and largest for the samples with lowest (50%) porosity. First maximum compressive strength in the stress-strain curve is followed by the oscillating section manifesting the onset of the cell deformation and partial collapse in the localized zone (Figs. 6 and 7). This section is followed by the extended plateau stretching from about 20% to about 60% relative compression. Increasing stress values at the end of the test correspond to the emergence of solidified section around the localized deformation area with completely collapsed cells behaving similar to the solid material section. This part of the test is not taken into account in the calculation of the test parameters according to the ISO 13314 standard. It is mainly determined by the fact that actual contact area of the sample at this stage start to deflect from the initial one, which is quite hard to take into account for the calculations needed. Relatively small size of the samples did not allow the use of the extensometer. For this reason, the precision of the small anvil displacement is not adequate, and possible calculations done for the elastic deformation area will have rather low precision. Table 3 presents typical values calculated from the compression tests of the samples according to the ISO 13314 standard. Relatively small numbers of tested samples did not allow full statistical analysis of the values and should be used indicatively.

Fig. 9 presents the dependences of the first maximum compressive strength σ_{max1} and the plateau stress σ_{pl} on the sample porosity P. Both curves behave quite consistently; the plateau stresses are 21 … 31% less than the first maximum one and their relative difference decreases with the increase of porosity.
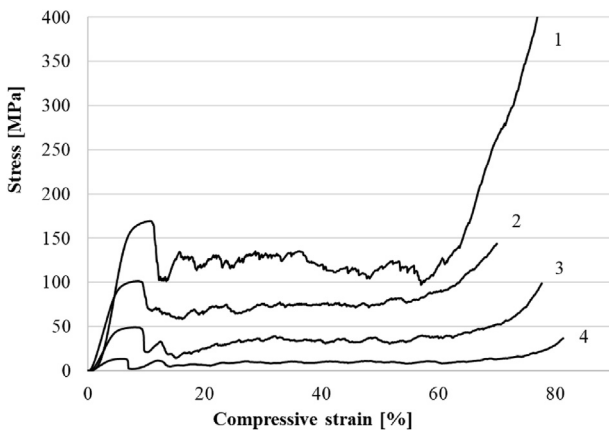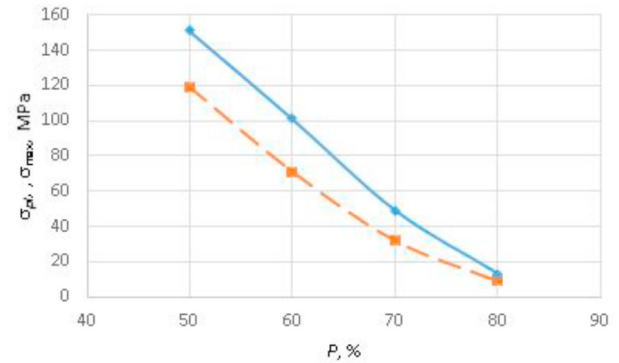

Fig. 9. The correlation of the first maximum compressive strength σ_{max1} (solid line) and the plateau stress σ_{pl} (dashed line) with the porosity P.

Fig. 10 presents the dependence of compressive offset stress $\sigma_{0.2}$ with the sample porosity of P. The compressive offset stress $\sigma_{0.2}$ decreases approximately 12 times in the porosity range of 50%–80%, which indicates a significant influence of porosity on this variable.

Energy absorption values (W) presented in Table 3 demonstrate expected decreasing tendency with increasing porosity of the samples. More critically, the energy absorption efficiency also demonstrate decreasing tendency with increasing porosity. Energy efficiency value for the sample with 60% porosity is falling below the trend line. Analysis of the video recording of the compression test clearly indicated certain difference in the deformation mechanism as compared to other samples. It is also possible to see comparing Figs. 6 and 7 sample with 60% porosity had a different angle of the thickening zone as compared to other samples.

The experiments showed that at some point an intense damage and partially shear band, which is inclined to the surface of the plates, occurs under compression quite similar to the observations
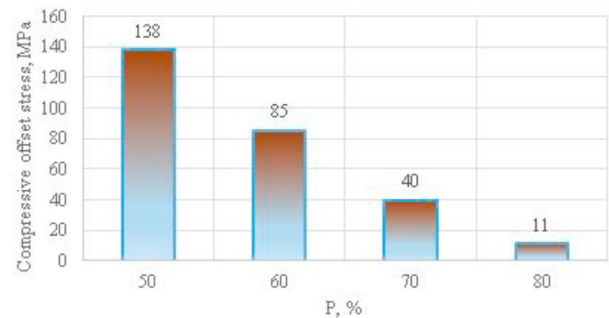

Fig. 8. Typical compressive stress dependences for the samples with different porosity relative porosity: 1–50%; 2–60%; 3–70%; 4–80%.

Fig. 10. The correlation of compressive offset stress $\sigma_{0.2}$ with sample porosity P.

Table 3
Parameters extracted from the typical compressive stress-relative compression curves.

Variables		Porosity P, %			
		50	60	70	80
Plateau stress σ_{pl}	MPa	119	71	32	9
First maximum compressive strength σ_{max1}	MPa	151	101	49	13
Plateau end e_{pl}	%	59	64	66	68
Compressive offset stress $\sigma_{0.2}$	%	138	85	40	11
Energy absorption W	MJ/m^3	58	35	15.5	4
Energy absorption efficiency	%	99	87	96	82

made by other researchers. In some instances, the bands looked like planes cutting across the body of the sample at an angle to the vertical axis close to 45°, similar to wat was reported by Soro et al. [49]. Sometimes the angle of the damage localization plane was quite large, similar to what was reported by Bobbert et al. [50]. Some authors reported on quite large damage bands, presenting whole region of intense shear. Authors of [50] also reported that compression process of the porous sample is accompanied by significant barrel distortion of the sample edges.

In our experiments, shape and inclination of the damage bands in the samples were inconsistent, which is schematically illustrated in Fig. 11.

According to continuum mechanics, shear bands form when the plates are situated at an angle of 45° under maximum shear stresses. The fact that the deformed medium is not continuous but cellular (metamaterial), needs to be taken into consideration as the continuity hypothesis does not any longer hold. In simple words, mechanical stress cannot be transmitted through metal-free pores. The deformation theory, commonly used for metal forming, does not apply to compressible media. However, the theory of stress state does not depend on compressibility. Therefore, one of the hypotheses explaining this phenomenon is the assumption that shear bands are located in the regions of maximum shear stresses. However, this is not always confirmed by experiments. For example, Öchsner et al. [51]. Proved that in the compression test of their cellular sample the shear band was localized along the horizontal plane.

It is also clear that the concept of contact surfaces used in abovementioned calculation is ubiquitous in the case of porous samples. Corresponding deformations of the sample sections adjacent to the anvil are changing with increasing loading, and bending elements of the cells significantly change the load transfer from the anvils to the sample as can be seen from Fig. 5. It may lead to the situations, when some of the cells partially or completely loose the contact with the anvils at some loading values and from time to time. That can lead to the excess loading of the other cells and lead to initiating the odd cell deformation and shear bands. The appearance of shear bands manifests the onset of the deformation localization. In the corresponding compression tests of the porous (lattice) samples that can lead to increasing stochastic component of damage and shear band generation. The same time in our tests, the direction of damage and sheer bands was from the top to bottom and left to right. This observation is pointing to certain deterministic factor in the damage and shear band formation. We hypothesized that deflection of the anvil surfaces contacting the

samples from true parallel arrangement at the increasing loads can be a possible reason for that. Similar effect can be caused by uneven top surface of the samples also leading to the nonevent contact of sample and compression anvils.

To test the feasibility of the "bad anvil contact" hypotheses additional modeling was undertaken using the Mechanical Structure module of ANSYS software. Corresponding boundary conditions were taken as described in the Materials and methods above, but sample models were modified to account for the uneven anvil contact. A number of cells were removed from the top and bottom corners of the structure (Fig. 12). Simulations were carried out for not exceptionally high loads, when there was no contact of the anvils with the lower laying cells in the "empty" corners.

Results of the simulation presented in Fig. 12 demonstrate that in the case of asymmetric contact of the anvils with the sample equivalent stresses are distributed unevenly. Fig. 13 demonstrates this effect more clearly displaying the field of equivalent strain. It shows a clear diagonal zone of the increased strain connecting the areas with no contact to the anvils. With further increase in the load, corresponding damage and shear band will form in the zone of increased strain shown in the figure.
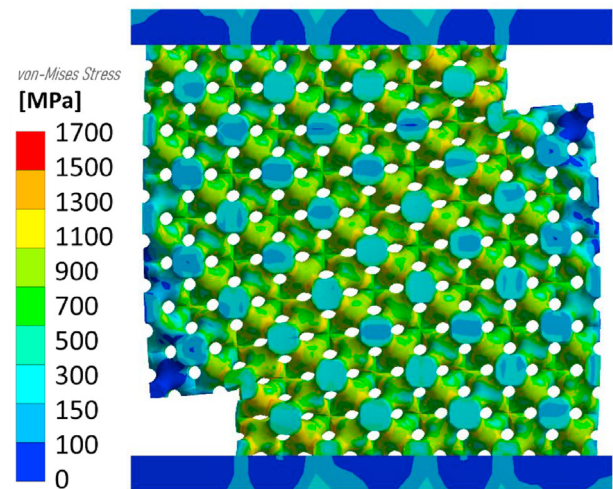

Fig. 12. The region of equivalent stresses in a sample with asymmetric cells.
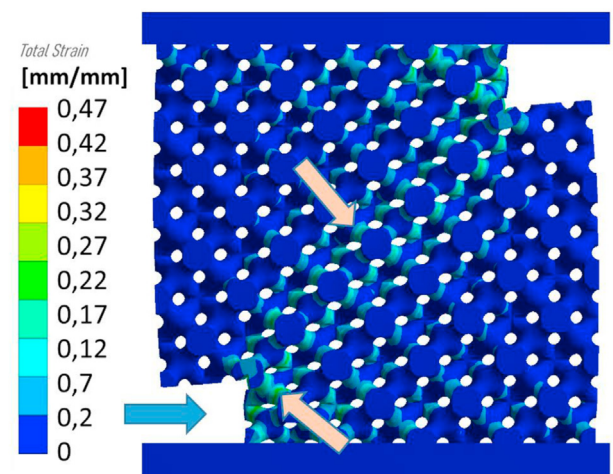

Fig. 13. The region of increased equivalent strain a predecessor of damage and shear band, forming due to the uneven contact with the compression anvils. Blue arrow points to the distortion of the originally square cut in the sample.
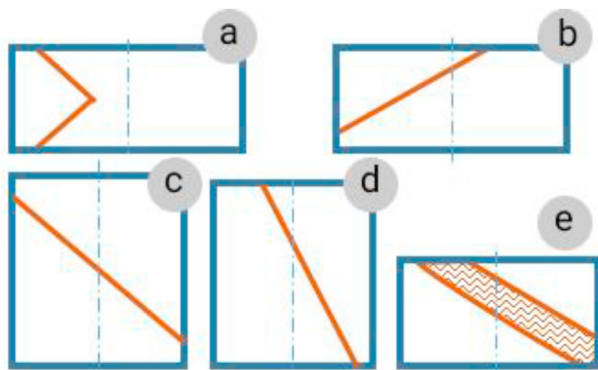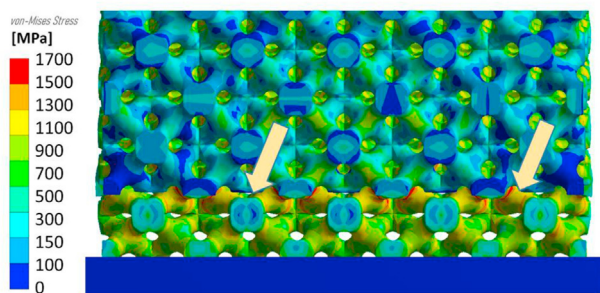

Fig. 11. Variations of the shear bands in the compressed samples: a — double; b-narrow extending to the contact and side surfaces; c-narrow extending to the side surfaces; d-narrow extending to the contact surfaces; e-wide extending to the contact and side surfaces.

Fig. 14. The field of equivalent stresses in the sample with uneven contact to the compression anvils, light arrows indicate the cut plane to the eliminated part of the sample (blue arrow in Fig. 13).

Fig. 14 presents the modelled side view of the loaded sample (from the direction of the blue arrow in Fig. 13). Corresponding cells that are not in contact with the compression anvils are clearly demonstrating much lower equivalent stress, which creates an additional heterogeneity in the stress distribution. As a result, the stress concentrates in the corners where the cells were eliminated causing larger deformations and their propagation in the diagonal direction.

4. Conclusions

Corresponding research was carried out to assess if the porous structures with modified diamond-shaped lattice cells can provide better integrity of the constructions in the case of overloading. Corresponding approach appears quite promising. Further studies will be aiming at better statistical analysis and optimization of the unit cell design for minimizing the susceptibility to local failure.

(1) The research of the compression deformation in cellular structures made of Ti–6Al–4V alloy with modified diamond-shape unit cells was carried out. The experimental and modeling results obtained showed that when the sample porosity rises from 50% to 80%, plateau stress decreases by 13 times. First maximum compressive strength decreases by 12 times, and Compression offset stress decreases by 12 times, while Plateau end does not change significantly.
(2) The experiments revealed certain, but not major barrel distortion of the edges of the samples, which is in line with other studies of the lattice sample compression.
(3) It is revealed that the deformation localizes in the form of damage and shear bands. Although positioning of such bands across the sample should be random, certain determinism was observed. Corresponding analysis indicates that one of determinism in predominant direction in the shear band is possible asymmetry of the contact between the sample and compression anvils.
(4) Approach of modifying the beam-based lattice cells is feasible in achieving the porous structures with higher tolerance to the overloading without catastrophic damage and loss of their integrity.
(5) To improve the fidelity of the measurements and guarantee uniform contact with the anvils one can consider using compression samples, where the porous layer is integrated between two solid metal layers. However, it is not clear, how the transient area between the porous and solid sections will influence the measured parameters attributed to only the porous part. Thus, corresponding comparison experiments will be needed.

Data availability statement

Data can be accessed from https://www.dropbox.com/s/5mnlld5wre5n89y/Ru%20Lattice.rar?dl=0.

Conflicts of interest

The authors declare that there is no conflicts of interest.

Acknowledgements

References

[1] J. Tokarczyk, M. Dudek, O. Jordá, E. Martinez, A. Peñuelas-Herráiz, V.-J. Primo-Capella, OVOMAX online course as a way to improve competencies and qualifications for designing and manufacturing of custom-made orthopaedic implants, in: S. Nazir, A.-M. Teperi, A. Polak-Sopińska (Eds.), BT - Advances in Human Factors in Training, Education, and Learning Sciences, Springer International Publishing, Cham, 2019, pp. 362–374.
[2] C. Zhang, J. Lin, H. Liu, Magnesium-based biodegradable materials for biomedical applications, MRS Adv 3 (2018) 2359–2364, https://doi.org/10.1557/adv.2018.488.
[3] H. Shen, H. Li, L.C. Brinson, Effect of microstructural configurations on the mechanical responses of porous titanium: a numerical design of experiment analysis for orthopedic applications, Mech. Mater. 40 (2008) 708–720, https://doi.org/10.1016/j.mechmat.2008.03.009.
[4] M. Geetha, A.K. Singh, R. Asokamani, A.K. Gogia, Ti based biomaterials, the ultimate choice for orthopaedic implants – a review, Prog. Mater. Sci. 54 (2009) 397–425, https://doi.org/10.1016/j.pmatsci.2008.06.004.
[5] E. Chudinova, M. Surmeneva, A. Koptyug, P. Scoglund, R. Surmenev, Additive manufactured Ti6Al4V scaffolds with the RF- magnetron sputter deposited hydroxyapatite coating, in: J. Phys. Conf. Ser., 2016, https://doi.org/10.1088/1742-6596/669/1/012004, 0–6.
[6] M.A. Surmeneva, A. Koptyug, D. Khrapov, Y.F. Ivanov, T. Mishurova, S. Evsevleev, O. Prymak, K. Loza, M. Epple, G. Bruno, R.A. Surmenev, In situ synthesis of a binary Ti–10at% Nb alloy by electron beam melting using a mixture of elemental niobium and titanium powders, J. Mater. Process. Technol. 282 (2020) 116646, https://doi.org/10.1016/j.jmatprotec.2020.116646.
[7] H. Li, M. Wang, D. Lou, W. Xia, X. Fang, Microstructural features of biomedical cobalt–chromium–molybdenum (CoCrMo) alloy from powder bed fusion to aging heat treatment, J. Mater. Sci. Technol. 45 (2020) 146–156, https://doi.org/10.1016/j.jmst.2019.11.031.
[8] M. Tilton, G.S. Lewis, G.P. Manogharan, in: B. Li, T. Webster (Eds.), Additive Manufacturing of Orthopedic Implants BT - Orthopedic Biomaterials : Progress in Biology, Manufacturing, and Industry Perspectives, Springer International Publishing, Cham, 2018, pp. 21–55, https://doi.org/10.1007/978-3-319-89542-0_2.
[9] K. Willemsen, R. Nizak, H.J. Noordmans, R.M. Castelein, H. Weinans, M.C. Kruyt, Challenges in the design and regulatory approval of 3D-printed surgical implants: a two-case series, Lancet Digit. Health 1 (2019) e163–e171, https://doi.org/10.1016/S2589-7500(19)30067-6.
[10] E. Kudryavtseva, V. Popov, G. Muller-Kamskii, E. Zakurinova, V. Kovalev, Advantages of 3D printing for gynecology and obstetrics: brief review of applications, technologies, and prospects, in: 2020 IEEE 10th Int. Conf. Nanomater. Appl. Prop., 2020, https://doi.org/10.1109/NAP51477.2020.9309602, 02SAMA09-1-02SAMA09-5.
[11] F.R. Kaschel, M. Celikin, D.P. Dowling, Effects of laser power on geometry, microstructure and mechanical properties of printed Ti-6Al-4V parts, J. Mater. Process. Technol. 278 (2020) 116539, https://doi.org/10.1016/j.jmatprotec.2019.116539.
[12] V.V. Popov Jr., A. Katz-Demyanetz, A. Kovalevsky, R. Biletskiy, E. Strokin, A. Garkun, M. Bamberger, V. Popov, A. Katz-Demyanetz, A. Kovalevsky, et al., Effect of the hatching strategies on mechanical properties and microstructure of SEBM manufactured Ti-6Al-4V specimens, Lett. Mater. 8 (2018) 468–472, https://doi.org/10.22226/2410-3535-2018-4-468-472.
[13] V.V. Popov, M.L. Lobanov, S.I. Stepanov, Y. Qi, G. Muller-Kamskii, E.N. Popova, A. Katz-Demyanetz, A.A. Popov, Texturing and phase evolution in Ti-6Al-4V: effect of electron beam melting process, powder Re-using, and HIP treatment, Materials 14 (2021), https://doi.org/10.3390/ma14164473.
[14] V. Popov, A. Katz-Demyanetz, M. Bamberger, Heat transfer and phase formation through EBM 3D-printing of Ti-6Al-4V cylindrical parts, Defect Diffusion Forum 383 (2018) 190–195. www.scientific.net/DDF.383.190, 10.4028.

[15] Z. Wang, M. Liu, Dimensionless analysis on selective laser melting to predict porosity and track morphology, J. Mater. Process. Technol. 273 (2019) 116238, https://doi.org/10.1016/j.jmatprotec.2019.05.019.

[16] G. Del Guercio, M. Galati, A. Saboori, Innovative approach to evaluate the mechanical performance of Ti–6Al–4V lattice structures produced by electron beam melting process, Met. Mater. Int. 27 (2021) 55–67, https://doi.org/10.1007/s12540-020-00745-2.

[17] P. Prochor, L. Frossard, E. Sajewicz, Effect of the material's stiffness on stress-shielding in osseointegrated implants for bone-anchored prostheses: a numerical analysis and initial benchmark data, Acta Bioeng. Biomech. 22 (2020), https://doi.org/10.37190/abb-01543-2020-02.

[18] M.A. Surmeneva, R.A. Surmenev, E.A. Chudinova, A. Koptioug, M.S. Tkachev, S.N. Gorodzha, L.-E. Rännar, Fabrication of multiple-layered gradient cellular metal scaffold via electron beam melting for segmental bone reconstruction, Mater. Des. 133 (2017) 195–204, https://doi.org/10.1016/j.matdes.2017.07.059.

[19] L. Yang, M. Ferrucci, R. Mertens, W. Dewulf, C. Yan, Y. Shi, S. Yang, An investigation into the effect of gradients on the manufacturing fidelity of triply periodic minimal surface structures with graded density fabricated by selective laser melting, J. Mater. Process. Technol. 275 (2020) 116367, https://doi.org/10.1016/j.jmatprotec.2019.116367.

[20] A. Bandyopadhyay, F. Espana, V.K. Balla, S. Bose, Y. Ohgami, N.M. Davies, Influence of porosity on mechanical properties and in vivo response of Ti6Al4V implants, Acta Biomater. 6 (2010) 1640–1648, https://doi.org/10.1016/j.actbio.2009.11.011.

[21] L. Liu, S. Wang, J. Liu, F. Deng, Z. Li, Y. Hao, Architectural design of Ti6Al4V scaffold controls the osteogenic volume and application area of the scaffold, J. Mater. Res. Technol. 9 (2020) 15849–15861, https://doi.org/10.1016/j.jmrt.2020.11.061.

[22] M. de Wild, R. Schumacher, K. Mayer, E. Schkommodau, D. Thoma, M. Bredell, A. Kruse Gujer, K.W. Grätz, F.E. Weber, Bone regeneration by the osteoconductivity of porous titanium implants manufactured by selective laser melting: a histological and micro computed tomography study in the rabbit, Tissue Eng. 19 (2013) 2645–2654, https://doi.org/10.1089/ten.tea.2012.0753.

[23] V. Popov, G. Muller-Kamskii, A. Katz-Demyanetz, A. Kovalevsky, S. Usov, D. Trofimcow, G. Dzhenzhera, A. Koptyug, Additive manufacturing to veterinary practice: recovery of bony defects after the osteosarcoma resection in canines, Biomed. Eng. Lett. 9 (2019) 97–108, https://doi.org/10.1007/s13534-018-00092-7.

[24] D. Khrapov, A. Koptyug, K. Manabaev, F. Léonard, T. Mishurova, G. Bruno, D. Cheneler, K. Loza, M. Epple, R. Surmenev, M. Surmeneva, The impact of post manufacturing treatment of functionally graded Ti6Al4V scaffolds on their surface morphology and mechanical strength, J. Mater. Res. Technol. 9 (2020) 1866–1881, https://doi.org/10.1016/j.jmrt.2019.12.019.

[25] S. Evsevleev, T. Mishurova, D. Khrapov, A. Paveleva, D. Meinel, R. Surmenev, M. Surmeneva, A. Koptyug, G. Bruno, X-ray computed tomography procedures to quantitatively characterize the morphological features of triply periodic minimal surface structures, Materials 14 (2021), https://doi.org/10.3390/ma14113002.

[26] A.I. Golodnov, Y.N. Loginov, S.I. Stepanov, Numeric loading simulation of titanium implant manufactured using 3D printing, Solid State Phenom. 284 (2018) 380–385. www.scientific.net/SSP.284.380, 10.4028.

[27] H. Mehboob, F. Tarlochan, A. Mehboob, S.-H. Chang, Finite element modelling and characterization of 3D cellular microstructures for the design of a cementless biomimetic porous hip stem, Mater. Des. 149 (2018) 101–112, https://doi.org/10.1016/j.matdes.2018.04.002.

[28] Y. Chen, J.E. Frith, A. Dehghan-Manshadi, H. Attar, D. Kent, N.D.M. Soro, M.J. Bermingham, M.S. Dargusch, Mechanical properties and biocompatibility of porous titanium scaffolds for bone tissue engineering, J. Mech. Behav. Biomed. Mater. 75 (2017) 169–174, https://doi.org/10.1016/j.jmbbm.2017.07.015.

[29] H.M.A. Kolken, S. Janbaz, S.M.A. Leeflang, K. Lietaert, H.H. Weinans, A.A. Zadpoor, Rationally designed meta-implants: a combination of auxetic and conventional meta-biomaterials, Mater. Horiz. 5 (2018) 28–35, https://doi.org/10.1039/C7MH00699C.

[30] C.P. de Jonge, H.M.A. Kolken, A.A. Zadpoor, Non-Auxetic mechanical meta-materials, Materials 12 (2019), https://doi.org/10.3390/ma12040635.

[31] S. Daynes, J. Lifton, W.F. Lu, J. Wei, S. Feih, Fracture toughness characteristics of additively manufactured Ti–6Al–4V lattices, Eur. J. Mech. Solid. 86 (2021) 104170, https://doi.org/10.1016/j.euromechsol.2020.104170.

[32] K. Yang, J. Wang, L. Jia, G. Yang, H. Tang, Y. Li, Additive manufacturing of Ti-6Al-4V lattice structures with high structural integrity under large compressive deformation, J. Mater. Sci. Technol. 35 (2019) 303–308, https://doi.org/10.1016/j.jmst.2018.10.029.

[33] D. Zhao, Y. Huang, Y. Ao, C. Han, Q. Wang, Y. Li, J. Liu, Q. Wei, Z. Zhang, Effect of pore geometry on the fatigue properties and cell affinity of porous titanium scaffolds fabricated by selective laser melting, J. Mech. Behav. Biomed. Mater. 88 (2018) 478–487, https://doi.org/10.1016/j.jmbbm.2018.08.048.

[34] Q. Ran, W. Yang, Y. Hu, X. Shen, Y. Yu, Y. Xiang, K. Cai, Osteogenesis of 3D printed porous Ti6Al4V implants with different pore sizes, J. Mech. Behav. Biomed. Mater. 84 (2018) 1–11, https://doi.org/10.1016/j.jmbbm.2018.04.010.

[35] L.E. Murr, W.L. Johnson, 3D metal droplet printing development and advanced materials additive manufacturing, J. Mater. Res. Technol. 6 (2017) 77–89, https://doi.org/10.1016/j.jmrt.2016.11.002.

[36] S.H. Teoh, R. Thampuran, W.K.H. Seah, J.C.H. Goh, Effect of pore sizes and cholesterol-lipid solution on the fracture toughness of pure titanium sintered compacts, Biomaterials 14 (1993) 407–412, https://doi.org/10.1016/0142-9612(93)90142-O.

[37] H. Shen, S.M. Oppenheimer, D.C. Dunand, L.C. Brinson, Numerical modeling of pore size and distribution in foamed titanium, Mech. Mater. 38 (2006) 933–944, https://doi.org/10.1016/j.mechmat.2005.06.027.

[38] D. Ren, S. Li, H. Wang, W. Hou, Y. Hao, W. Jin, R. Yang, R.D.K. Misra, L.E. Murr, Fatigue behavior of Ti-6Al-4V cellular structures fabricated by additive manufacturing technique, J. Mater. Sci. Technol. 35 (2019) 285–294, https://doi.org/10.1016/j.jmst.2018.09.066.

[39] F. Bartolomeu, M.M. Costa, J.R. Gomes, N. Alves, C.S. Abreu, F.S. Silva, G. Miranda, Implant surface design for improved implant stability – a study on Ti6Al4V dense and cellular structures produced by Selective Laser Melting, Tribol. Int. 129 (2019) 272–282, https://doi.org/10.1016/j.triboint.2018.08.012.

[40] A. du Plessis, C. Broeckhoven, I. Yadroitsava, I. Yadroitsev, C.H. Hands, R. Kunju, D. Bhate, Beautiful and functional: a review of biomimetic design in additive manufacturing, Addit. Manuf. 27 (2019) 408–427, https://doi.org/10.1016/J.ADDMA.2019.03.033.

[41] H. Attar, S. Ehtemam-Haghighi, D. Kent, X. Wu, M.S. Dargusch, Comparative study of commercially pure titanium produced by laser engineered net shaping, selective laser melting and casting processes, Mater. Sci. Eng. 705 (2017) 385–393, https://doi.org/10.1016/j.msea.2017.08.103.

[42] N. Taniguchi, S. Fujibayashi, M. Takemoto, K. Sasaki, B. Otsuki, T. Nakamura, T. Matsushita, T. Kokubo, S. Matsuda, Effect of pore size on bone ingrowth into porous titanium implants fabricated by additive manufacturing: an in vivo experiment, Mater. Sci. Eng. C 59 (2016) 690–701, https://doi.org/10.1016/j.msec.2015.10.069.

[43] V.V. Popov, G. Muller-Kamskii, A. Kovalevsky, G. Dzhenzhera, E. Strokin, A. Kolomiets, J. Ramon, et al., Design and 3D-printing of titanium bone implants: brief review of approach and clinical cases, Biomed. Eng. Lett. 8 (2018) 337–344, https://doi.org/10.1007/s13534-018-0080-5.

[44] N. Eliaz, N. Foucks, D. Geva, S. Oren, N. Shriki, D. Vaknin, D. Fishman, O. Levi, Comparative quality control of titanium alloy Ti–6Al–4V, 17–4 PH stainless steel, and aluminum alloy 4047 either manufactured or repaired by laser engineered net shaping (LENS), Materials 13 (2020), https://doi.org/10.3390/ma13184171.

[45] A.-F. Obaton, J. Fain, M. Djemaï, D. Meinel, F. Léonard, E. Mahé, B. Lécuelle, J.-J. Fouchet, G. Bruno, In vivo XCT bone characterization of lattice structured implants fabricated by additive manufacturing, Heliyon 3 (2017), e00374, https://doi.org/10.1016/j.heliyon.2017.e00374.

[46] International Organization for Standardization, ISO 13314:2011 Mechanical Testing of Metals – Ductility Testing – Compression Test for Porous and Cellular Metals, 2011. www.iso.org.

[47] Y. Loginov, S. Stepanov, C. Khanykova, Inhomogeneity of deformed state during compression testing of titanium implant, in: MATEC Web Conf., 2017, https://doi.org/10.1051/matecconf/201713203009.

[48] H.E. Burton, N.M. Eisenstein, B.M. Lawless, P. Jamshidi, M.A. Segarra, O. Addison, D.E.T. Shepherd, M.M. Attallah, L.M. Grover, S.C. Cox, The design of additively manufactured lattices to increase the functionality of medical implants, Mater. Sci. Eng. C 94 (2019) 901–908, https://doi.org/10.1016/j.msec.2018.10.052.

[49] N. Soro, H. Attar, X. Wu, M.S. Dargusch, Investigation of the structure and mechanical properties of additively manufactured Ti-6Al-4V biomedical scaffolds designed with a Schwartz primitive unit-cell, Mater. Sci. Eng. 745 (2019) 195–202, https://doi.org/10.1016/j.msea.2018.12.104.

[50] F.S.L. Bobbert, K. Lietaert, A.A. Eftekhari, B. Pouran, S.M. Ahmadi, H. Weinans, A.A. Zadpoor, Additively manufactured metallic porous biomaterials based on minimal surfaces: a unique combination of topological, mechanical, and mass transport properties, Acta Biomater. 53 (2017) 572–584, https://doi.org/10.1016/j.actbio.2017.02.024.

[51] A. Öchsner, K. Lamprecht, On the uniaxial compression behavior of regular shaped cellular metals, Mech. Res. Commun. 30 (2003) 573–579, https://doi.org/10.1016/S0093-6413(03)00058-2.